KeA1

CHINESE ROOTS
GLOBAL IMPACT

#### Contents lists available at ScienceDirect

#### Petroleum Science

journal homepage: www.keaipublishing.com/en/journals/petroleum-science



#### Original Paper

### Stress corrosion cracking behavior of buried oil and gas pipeline steel under the coexistence of magnetic field and sulfate-reducing bacteria



Jian-Yu He a, b, Fei Xie a, b, \*, Dan Wang a, b, Guang-Xin Liu c, \*\*, Ming Wu a, b, Yue Qin d

- <sup>a</sup> College of Petroleum Engineering, Liaoning Petrochemical University, Fushun, 113001, Liaoning, China
- b Key Laboratory of Oil and Gas Storage and Transportation Technology in Liaoning Province, Fushun, 113001, Liaoning, China
- c State Key Joint Laboratory of Environment Simulation and Pollution Control, School of Environment, Tsinghua University, Beijing, 100084, China
- <sup>d</sup> PipeChina West East Gas Pipeline Company, Shanghai, 200120, China

#### ARTICLE INFO

# Article history: Received 19 October 2022 Received in revised form 31 July 2023 Accepted 16 October 2023 Available online 23 October 2023

Edited by Jia-Jia Fei and Min Li

Keywords: Magnetic field Sulfate-reducing bacteria Film layer Stress corrosion cracking Oil and gas pipelines

#### ABSTRACT

Magnetic field and microorganisms are important factors influencing the stress corrosion cracking (SCC) of buried oil and gas pipelines. Once SCC occurs in buried pipelines, it will cause serious hazards to the soil environment. The SCC behavior of X80 pipeline steel under the magnetic field and sulfate-reducing bacteria (SRB) environment was investigated by immersion tests, electrochemical tests, and slow strain rate tensile (SSRT) tests. The results showed that the corrosion and SCC sensitivity of X80 steel decreased with increasing the magnetic field strength in the sterile environment. The SCC sensitivity was higher in the biotic environment inoculated with SRB, but it also decreased with increasing magnetic field strength, which was due to the magnetic field reduces microbial activity and promotes the formation of dense film layer. This work provided theoretical guidance on the prevention of SCC in pipeline steel under magnetic field and SRB coexistence.

© 2023 The Authors. Publishing services by Elsevier B.V. on behalf of KeAi Communications Co. Ltd. This is an open access article under the CC BY-NC-ND license (http://creativecommons.org/licenses/by-nc-nd/

#### 1. Introduction

With the increasing demand for long-distance oil and gas transmission in recent years, high-grade pipeline steel, especially X80 pipeline steel, is being used more and more widely. Nevertheless, the thin walls of high-grade pipeline steels are prone to stress corrosion cracking (SCC) (Cheng, 2013; Liu et al., 2017; Ma et al., 2020). SCC is one of the most destructive forms of corrosion failure, causing great harm and threatening both environmental and social safety (Ramamurthy and Atrens, 2013; Niazi et al., 2021). In the 1960s, fires, and explosions in high-pressure natural gas pipelines in Louisiana, USA, were caused by SCC in gas transmission pipelines (Song, 2010). Accordingly, the SCC problem of pipelines has attracted a lot of attention and it is also important to study the SCC behavior of pipelines to prevent the occurrence of SCC in pipelines.

Most oil and gas pipelines are buried in soil and microorganism

E-mail addresses: xiefei0413@163.com (F. Xie), guangxinliu2022@126.com (G.-X. Liu).

is one of the most important influencing factors in soil, where sulfate-reducing bacteria (SRB) is the most representative bacterial (Wang et al., 2017). SRB can cause pitting on the material surface. which is the origin of SCC (Wang et al., 2017; Liu and Cheng, 2020; Wei et al., 2021). SRB also forms biofilm on the material surface, the biofilm is an important factor in the material corrosion (Dou et al., 2018; Unsal et al., 2021; Yang et al., 2022). Numerous studies reported the effect of SRB, stress, and cathodic protection potential on SCC (Wu et al., 2014; Wang et al., 2021; Xie et al., 2021). Most of the reports suggested higher SCC sensitivity caused by SRB. To ensure the pipeline safety, the Magnetic Fluxleakage Testing (MFT) is required. After MFT, remanence can exist for weeks (Jackson et al., 2006; Su et al., 2022). Hence the effect of the remanence on the corrosion cannot be ignored. The magnetic field affects pipeline corrosion mainly through Lorentz force and magnetic field gradient force (Lu et al., 2010; Monzon and Coey, 2014; Zhao et al., 2021), which can also be explained by Magnetohydrodynamic theory (MHD) (Ručinskien et al., 2002; Zhang et al., 2021; Parapurath et al., 2021). Zhao et al. (2021) reported the effect of magnetic fields on the SCC of Fe<sub>83</sub>Ga<sub>17</sub> alloy.

The material corrosion under magnetic field and SRB condition has been reported extensively. Chen et al. (2014) and Liu et al.

<sup>\*</sup> Corresponding author.

<sup>\*\*</sup> Corresponding author.

(2016) investigated the corrosion behavior of metals when magnetic fields coexisted with the SRB. They found that the magnetic field hindered the growth of SRB and promoted the formation of more dense corrosion product films, which inhibited microbialinduced corrosion. Liu et al. (2018) suggested that the magnetic field and the extracellular polymer (EPS) of bacteria have a synergistic effect on corrosion, accelerating the corrosion of metals. It should be noted that the magnetic field also reduces the number of SRB cells in the environment, which has an impact on microbialinduced corrosion. Zheng et al. (2014) investigated the effect of static magnetic fields on SRB-induced corrosion of 304 stainless steel. The static magnetic field reduced the planktonic cells by about 10,000 times, retarded the formation of SRB biofilm on the stainless steel surface. Fojt et al. (2010) found magnetic elements are present in the active proteins and enzymes of bacteria and that magnetic fields affect the direction and speed of ion movement in solution. Only Li et al. (2021) have so far found a synergistic effect of magnetic field and SRB on the SCC of pipeline steel. They found that the magnetic field together with SRB accelerated SCC in the magnetic field range of 0-20 mT, while the SCC sensitivity decreased when the magnetic field increased to 30 mT. From these works, it is clear that magnetic fields can affect corrosion by influencing the growth and number of SRBs or biofilms on metal surfaces. Whether magnetic fields and SRB accelerate the corrosion of metals is, however, not yet conclusive. More importantly, most of the studies only focus on the effect of magnetic field and SRB on metal surface corrosion, and rarely cover the SCC behavior and mechanism of metals when magnetic field and SRB coexist. The magnetic field strength range of existing studies is also not close enough to the actual situation to provide good guidance for the prevention of SCC in actual pipelines.

In this work, the SCC behavior and mechanism of X80 pipeline steel under the coexistence of magnetic field and SRB in the soil environment was investigated. The corrosion morphology of X80 steel specimens was studied by scanning electron microscopy (SEM). Slow strain rate tensile (SSRT) tests were performed in sterile and SRB-inoculated soil-simulating solution at different magnetic field strengths. The fracture morphology of the specimens after fracture was analyzed using SEM. The findings of this paper contribute to the better application of leakage magnetic detection technology in the field of oil and gas pipelines in the future.

#### 2. Experiments

#### 2.1. Experimental materials

The main material for this work is X80 pipeline steel, whose elemental composition is listed in Table 1. All experimental specimens were cut from X80 steel retrieved from the site. The working surfaces of all experimental specimens were sanded smooth with 80~2000# water-based sandpaper, then cleaned with deionized water, dehydrated with anhydrous ethanol, and then dried in cold air. The experimental specimens were all sterilized under UV light for 25–30 min before the start of the experiment.

#### 2.2. Experimental solutions

The experimental solutions for this work included both sterile and SRB-inoculated Shenyang soil-simulating solutions. The composition of the Shenyang soil solution is given in Table 2. The pH of the simulated solution was adjusted to  $7.2 \pm 0.2$  using 5% glacial acetic acid and 5% NaOH solutions (both v/v). Solution preparation methods are presented here.

- (1) Sterile solution preparation: The sterile solution was prepared by mixing the Shenyang soil solution and SRB special media in a 1:1 ratio. All solutions were prepared with deionized water, to which nitrogen was passed for more than 30 min to remove the oxygen before the solution was prepared. Medium I and Medium II made up the SRB special medium (recommended by API). K<sub>2</sub>HPO<sub>4</sub> 0.5 g, CaCl<sub>2</sub> 0.1 g, Na<sub>2</sub>SO<sub>4</sub> 0.5 g, MgSO<sub>4</sub>•7H<sub>2</sub>O 2.0 g, NH<sub>4</sub>Cl 1.0 g, sodium lactate 3 mL, yeast powder 1.0 g, and 500 mL deionized water made up Medium I. The Medium I and solution were autoclaved at 121 °C for 15 min before use. Medium II consisted of insurance powder 0.1 g, ferrous ammonium sulfate 0.1 g, ascorbic acid 0.1 g, and 500 mL deionized water, sterilized by UV light for 30 min before use. SRB special medium was made by mixing sterilized Medium I and Medium II in equal proportions. Finally, the Shenyang soil solution was mixed with SRB special medium in equal proportions to make a sterile solution and used as a control.
- (2) Preparation of inoculated SRB soil simulation solution: The SRB strain (Desulfovibrio desulfuricans) used in this study was isolated and purified from Shenyang soil, and the procedure may be found in the group's prior works (Li et al., 2021). SRB strains of 4 days old were inoculated into blue-capped bottles (According to the actual amount of bacteria in Shenyang soil, the proportion of SRB strains inoculated was 1%.) containing sterile solution. After sealing it well, it was incubated in a biochemical incubator at 35  $\pm$  1 °C to ensure normal growth and metabolism of SRB. The Nd-Fe-B permanent magnets were placed on both sides of the bottle to simulate a magnetic field environment, and the magnitude of the magnetic field strength was controlled by varying the number and distance of the magnets (0, 25, 50, 75 and 100 mT). The magnitude of the magnetic field strength was controlled by varying the number and distance of the NdFeB permanent magnets. The experimental solution was guaranteed to be completely exposed to the magnetic field environment. The same magnetic environment settings were guaranteed for all experiments. Instruments used in the experiment, such as blue-capped bottles, glass rods, and beakers, were steam sterilized for 15-20 min in a steam autoclave at 121 °C or for more than 30 min under UV light. All of the experimental preparation work is done in a sterile setting.

**Table 2** Composition of Shenyang soil solution.

Ingredient	Ingredient MgSO <sub>4</sub> ·7H <sub>2</sub> O		NaHCO <sub>3</sub>	CaCl <sub>2</sub>	Na <sub>2</sub> SO <sub>4</sub>
Content, g/L	0.129	0.032	0.160	0.032	0.179

**Table 1** Elemental composition of X80 steel (wt%).

С	Si	Mn	P	S	В	Мо	Ni	Cr	Cu	Fe
0.044	0.19	1.83	0.011	0.002	0.0003	0.09	0.23	0.025	0.13	Balance

#### 2.3. Immersion experiments

The  $18 \times 10 \times 2 \text{ mm}^3$  specimens were immersed in the solution inoculated with SRB. The direction of the applied magnetic field was perpendicular to the working surface of the specimen. The specimens were immersed for 4 d. The morphology and composition of the surface films on the immersed specimens were then analyzed using a Hitachi SU8010 scanning electron microscope and energy spectrometer (EDS). The immersed specimens were cured for 8 h in a phosphate buffer containing 2.5% glutaraldehyde before being analyzed. The film was then dehydrated for 8 min in 50%, 60%, 70%, 80%, 90%, 95%, and 100% ethanol solutions, dried with a cold wind, and sprayed with a thin layer of platinum powder to increase the film's electrical conductivity, before being examined by SEM. Moreover, the number of SRBs adhering to the surface of the specimen at different magnetic field strengths on day 4 was measured by the blood cell counting plate method (Xian et al., 2010).

#### 2.4. Electrochemical experiments

The electrochemical impedance spectroscopy (EIS) test device and specimen are shown in Fig. 1. The specimen size is  $10 \times 10 \times 2$  mm<sup>3</sup>. Experimental tests are carried out by an electrochemical workstation (PARSTAT 4000A) with the magnetic field directed perpendicular to the working surface of the specimen. The specimen, platinum sheet, and saturated calomel electrode were used as working electrode (WE), counter electrode (CE), and reference electrode (RE) in the electrochemical tests, respectively. The open-circuit potential was first monitored for a period of 3600 s to ensure its stability. Finally, EIS was performed at an open-circuit potential with a frequency of 100 kHz to 10 mHz, and a sinusoidal voltage signal with an amplitude of 10 mV. To ensure reproducibility, all tests were carried out in three parallel sets.

#### 2.5. Slow strain rate tensile tests (SSRT) experiments

The dimensions of the tensile specimens are shown in Fig. 4, according to the national standard GB/T 15970–2009. Tensile specimens were cut from X80 pipeline steel in the direction of the pipeline circumference (i.e., transverse direction) as shown in Fig. 2. Since the circumference of the pipeline is the direction where the

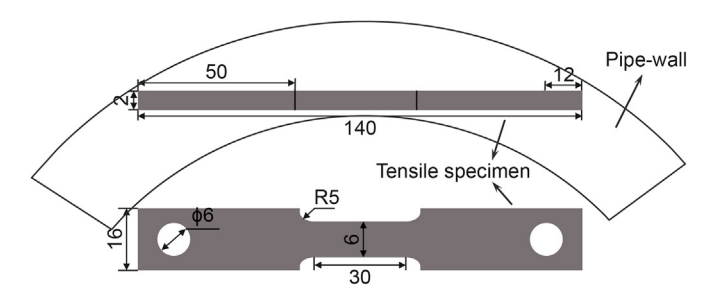


Fig. 2. Schematic diagram of cutting method of a tensile specimen.

maximum stress is generated by the pressure of the internally transported fluid, the circumference of the pipeline is selected for cutting.

Fig. 3 exhibits the SSRT experimental device that was used to test the SCC sensitivity of the specimens. To ensure the SRB's proper survival, the device was kept at a consistent temperature by a cryostat. The anaerobic environment required for SRB was provided by a removable sealed box. During the experiment, a magnetic field was applied on both sides of the specimen in a direction perpendicular to the specimen's surface, and the magnetic field strength was measured by a magnetic inductor (Fig. 4). The removable sealed box was divided into two layers, the inner layer held the

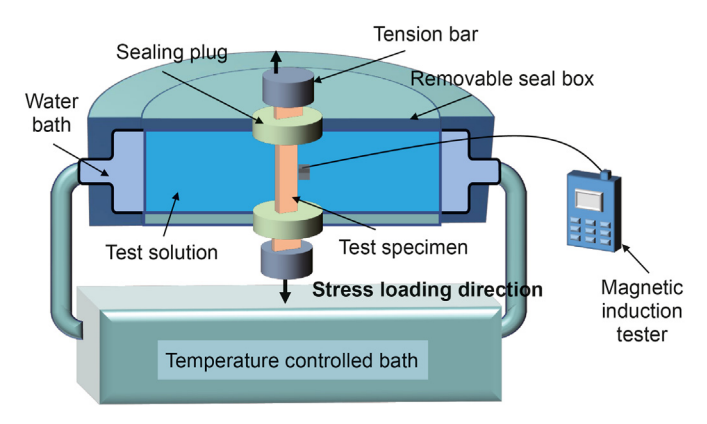


Fig. 3. Schematic of SSRT test device.

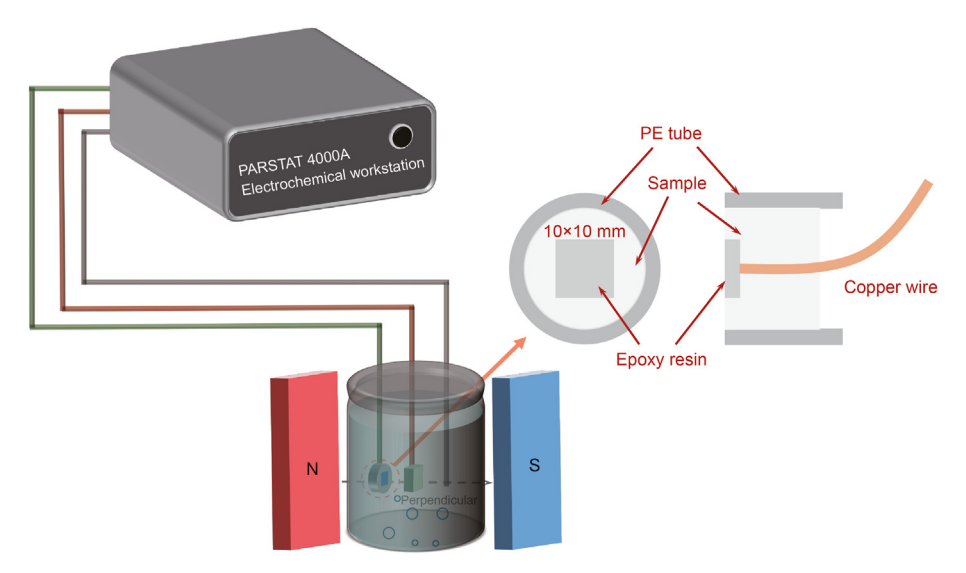


Fig. 1. Schematic of the electrochemical experimental device (with specimen dimensions).

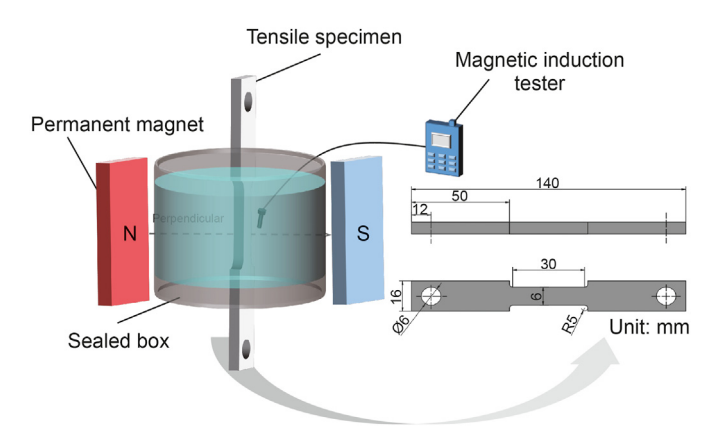


Fig. 4. Schematic of the stretched piece (with specimen dimensions).

experimental medium and the outer layer was filled with constant temperature water. Loading tensile specimens using the stress corrosion test system and applying a preload force of 420 N before the experiment starts, so that the specimens can be tightly connected to the instrument. Run the experiment at a strain rate of  $1 \times 10^{-6} \, \mathrm{s}^{-1}$  and record the load, displacement, and time during the experiment. After the SSRT experiment was completed, the fractured specimens were washed with anhydrous ethanol. The fracture morphologies were observed and analyzed by the SEM. All experiments were conducted in three parallel experiments.

#### 3. Results

#### 3.1. Effect of magnetic field on SRB

Fig. 5 shows the effect of the magnetic field on the number of SRB adsorbed on the surface of the specimen. The number of SRB adsorbed on the surface of the specimen declined as the magnetic field strength rose, reaching its lowest level at 100 mT. This result indicated that the magnetic field inhibited the growth of SRB on the surface of the specimen, which was similar to the results of Fojt et al. (2010).

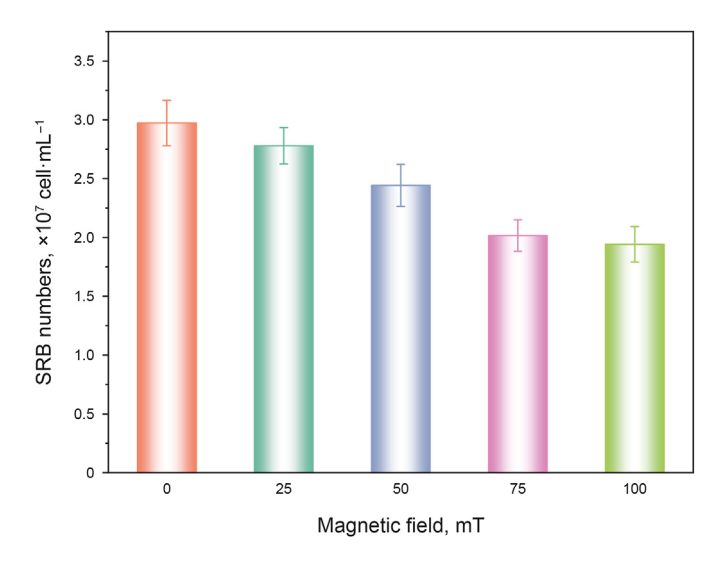


**Fig. 5.** Effect of different magnetic field strengths on the numbers of SRB adsorbed on the surface of the specimen.

#### 3.2. Biofilm characterization

In the solution inoculated with SRB, the SRB gradually adsorbed to the surface of the metal specimen and conducted life activities, which in turn secrete extracellular polymeric substances (EPS). EPS is attached to the metal surface, forming a film containing SRB covering the metal surface. Without a magnetic field, there were SRB strains (Fig. 6(a<sub>1</sub>) red arrow)) and obvious crack defects (Fig. 6(a<sub>1</sub>)) on the surface of the film layer, indicating that the layer was not sufficiently intact and compact. After a magnetic field was applied, the defects on the film layer gradually disappeared and the SRB strains on the surface gradually decreased. At 100 mT, no SRB was observed on the surface of the film which was flat and smooth at this moment. This indicated that the magnetic field enhanced the denseness and integrity of the film layer. The EDS results (Fig.  $6(a_1)$ ) and  $(e_1)$  indicated the presence of organic materials in the film layer. With no magnetic field, the high content of iron in the film indicated that the surface of the specimen had suffered severe corrosion. Furthermore, when a magnetic field was applied, the elemental sulfur content increased, implying that the magnetic field promoted the development of corrosion products such as iron sulfides.

#### 3.3. Electrochemical impedance spectroscopy (EIS)

Fig. 7 shows the EIS results and equivalent circuit diagrams. Fig. 7 ((a<sub>1</sub>), (a<sub>2</sub>)) and ((b<sub>1</sub>), (b<sub>2</sub>)) show the EIS results in the sterile solution environment and the inoculated SRB environment, respectively. EIS can be used to analyze data such as films and corrosion products produced by microbiological corrosion. The equivalent circuit is shown in the inset in Fig. 7(a<sub>1</sub>) and (b<sub>1</sub>), where  $R_s$  is the solution resistance,  $R_f$  is the resistance of the corrosion product film,  $Q_f$  is the corrosion product film,  $Q_d$  is the double layer capacitance,  $R_c$  is the charge transfer resistance and, W denotes the Warburg impedance. Replace the ideal capacitor C with the non-ideal interface capacitor Q.

$$Z_{\mathcal{Q}} = Y_{\mathcal{O}}(j\omega)^{-\alpha} \tag{1}$$

where  $Y_0$  and  $\alpha$  (which are departures from the ideal behavior) are CPE parameters and  $\omega$  is the angular frequency (rad/s).

The diameter of the semicircular arc in the sterile solution gradually increased as the magnetic field strength increased, as demonstrated in Fig.  $7(a_1)$ , implying the resistance to the corrosion reaction at the metal-solution interface increased, and corrosion was inhibited. A gradual straightening of the Nyquist curve was also observed in the low-frequency area of the semicircular arc, which may be due to the magnetic field affecting the migration of nutrients in the solution (Wan et al., 2019). In this situation, the equivalent circuit contained the Warburg impedance (Fig.  $7(a_1)$  inset), which appears precisely due to diffusion. The trend in the semicircular arcs was comparable to that in the sterile solution in the solution inoculated with SRB (Fig.  $7(b_1)$  and  $(b_2)$ ).

Table 3 displays the fitting parameters derived from the EIS results, all with error coefficients less than 10%, confirming the fitting process's great accuracy. Fig. 8 shows the fluctuation of the polarization resistance  $R_{\rm p}$  ( $R_{\rm p}=R_{\rm f}+R_{\rm ct}$ ) with magnetic field strength. The higher the polarization resistance value, the greater the corrosion resistance (Gong et al., 2020). The  $R_{\rm p}$  increased with increasing magnetic field strength in both the sterile and inoculated SRB environments, indicating that the magnetic field prevented the corrosion process, which is consistent with the results in Fig. 7. The  $R_{\rm p}$  in the inoculated SRB environment was lower than in the sterile condition, suggesting that the SRB accelerated the corrosion process.

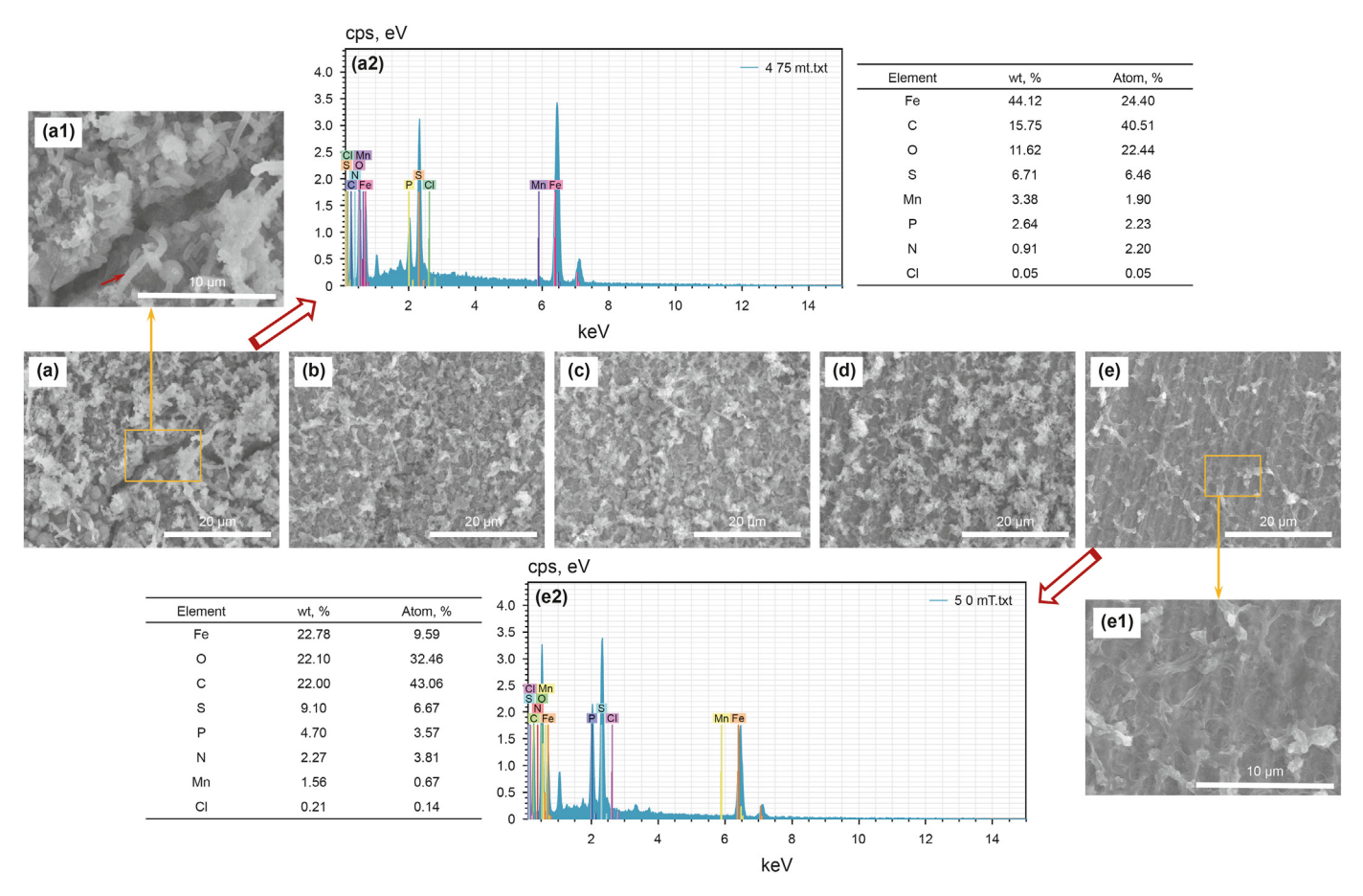


Fig. 6. Film micromorphology and EDS results on the surface of specimens after 4 d of immersion at different magnetic field strengths in the inoculated SRB environment: (a, a<sub>1</sub>, a<sub>2</sub>) 0 mT; (b) 25 mT; (c) 50 mT; (d)75 mT; (e, e<sub>1</sub>, e<sub>2</sub>) 100 mT. (a<sub>2</sub>, e<sub>2</sub>: EDS).

#### 3.4. SSRT results

Fig. 9 depicts the stress-strain curves, elongation, and crosssectional shrinkage of X80 steel specimens recorded in air and simulated sterile soil solutions. The yield strength measured in the air was 567 MPa, which is comparable to the yield strength recorded in sterile solutions at various magnetic field strengths. The fracture strains were all smaller than those in the air at varied magnetic field strengths, showing that the specimens are sensitive to stress corrosion. The fracture strain of the specimens gradually increased as the magnetic field strength increased (Fig. 9(a)), reaching a maximum of 100 mT, indicating that the perpendicular magnetic field can inhibit SCC. However, due to the elastic recovery of the specimen after fracture, the fracture strain cannot adequately reflect the specimen's SCC sensitivity (Javidi and Bahalaou Horeh, 2014). Elongation ( $\delta$ ) and cross-sectional shrinkage ( $\psi$ ) were therefore calculated and the results are shown in Fig. 9(b). The calculation equations are as follows.

$$\delta = \frac{L_1 - L_0}{L_0} \tag{2}$$

$$\psi = \frac{S_1 - S_0}{S_0} \tag{3}$$

where  $L_1$  is the specimen's length following fracture,  $L_0$  is the length before fracture,  $S_1$  is the cross-sectional area of the specimen following fracture, and  $S_0$  is the cross-sectional area before fracture.

The elongation ( $\delta_0$ ) and cross-sectional shrinkage ( $\psi_0$ ) measured in the air were 14.62% and 61.12% respectively, both greater than  $\delta$  and  $\psi$  for all other conditions. As shown in Fig. 9(b), elongation ( $\delta$ ) and cross-sectional shrinkage ( $\psi$ ) increase as the magnetic field strength increases (from 25 mT to 100 mT). This indicated that the SCC sensitivity of X80 steel decreases with increasing magnetic field strength, which has similarities with previous studies (Li et al., 2021)

Fig. 10 shows the results of SSRT in solution inoculated with SRB. Fig. 10(a) reveals that the magnetic field reduced the SCC sensitivity of X80 steel similar to the sterile solution. Fig. 10(b) shows the results for elongation and cross-sectional shrinkage. The regularity of variation of these two parameters was similar to that of the sterile environment, suggesting that the magnetic field also had an inhibiting effect on SCC in the inoculated SRB environment. The SCC sensitivity of X80 pipeline steel in a solution inoculated with SRB decreased with increasing magnetic field strength, similar to the results for the sterile environment (Fig. 9).

#### 3.5. Fracture morphology analysis

Fig. 11 shows the tensile fracture morphologies of X80 pipeline steel specimens in air and sterile solution at various magnetic field strengths. In the air, the macroscopic morphology (Fig. 11(a<sub>1</sub>)) revealed a dumbbell shape with a distinct necking phenomenon. The major fracture morphology (Fig. 11(a<sub>2</sub>)) demonstrated distinct dimple phenomena with uniform size. The specimens' side surfaces were smooth and flat, exhibiting typical ductile fracture

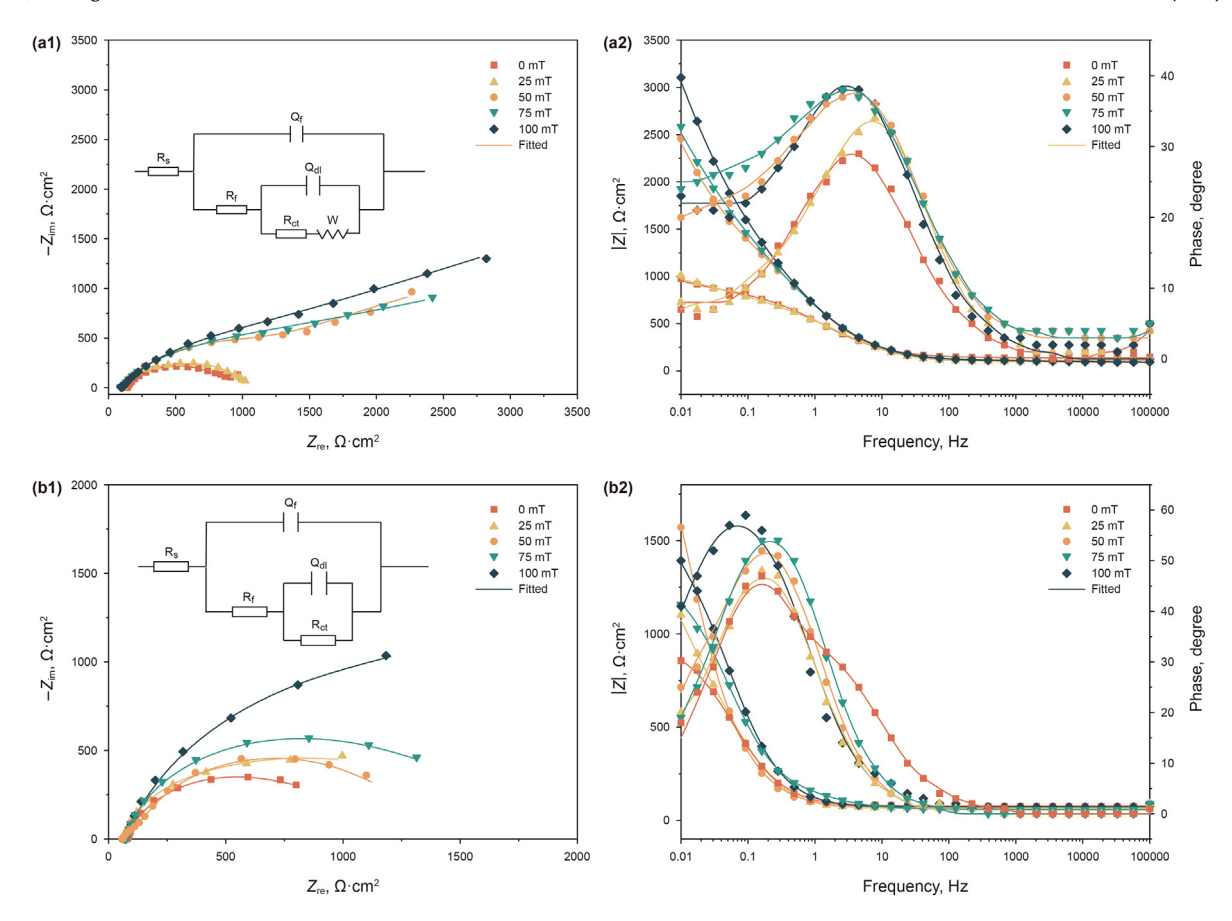


Fig. 7. EIS results for X80 steel in sterile solution (a<sub>1</sub>, a<sub>2</sub>) and solution inoculated with SRB (b<sub>1</sub>, b<sub>2</sub>) and the corresponding electrochemical equivalent circuit diagrams.

**Table 3**EIS fitting parameters (sterile and inoculated SRB).

	Magnetic field	$R_{\rm s}$	$Q_{\mathrm{f}}$	$R_{ m f}$	$Q_{dl}$	$R_{ct}$	W
Sterile environment	0 mT	120.3	$7.25 \times 10^{-4}$	49.95	2.46×10 <sup>-4</sup>	1348	$2.38 \times 10^{-2}$
	25 mT	111.4	$3.04 \times 10^{-4}$	65.08	$2.04 \times 10^{-4}$	1866	$0.16 \times 10^{-2}$
	50 mT	102.2	$1.53 \times 10^{-4}$	43.6	$10.47 \times 10^{-4}$	3547	$9.35 \times 10^{-2}$
	75 mT	50.27	$6.97 \times 10^{-4}$	70.13	$1.64 \times 10^{-4}$	4733	$1.18 \times 10^{-2}$
	100 mT	46.26	$4.67 \times 10^{-4}$	72.7	$2.20 \times 10^{-4}$	5796	$2.54 \times 10^{-2}$
With SRB	0 mT	64.99	3.57×10 <sup>-3</sup>	600.6	0.0307	750	
	25 mT	71.31	$4.32 \times 10^{-3}$	712.3	0.1271	1072	-
	50 mT	77.43	$3.67 \times 10^{-3}$	933	0.1332	1350	-
	75 mT	73.2	$2.53 \times 10^{-3}$	1374	0.0716	1589	-
	100 mT	58.4	$1.73 \times 10^{-3}$	2980.2	0.0015	2652	-

characteristics. The fractured specimen had a flat fracture surface with no necking without a magnetic field, and the major fracture appeared as a brittle fracture with a cleavage step (Fig. 11(b<sub>2</sub>)). The side surface (Fig. 11(b<sub>3</sub>)) displayed obvious secondary cracks oriented perpendicular to the direction of stress, indicating that the specimen was sensitive to SCC. After applying a magnetic field, the cleavage steps in the fractured specimen's major fracture progressively disappeared. When the magnetic field strength reaches 75 and 100 mT, the cleavage steps essentially disappear and inconspicuous dimples begin to appear. This indicated that the specimens began to exhibit ductile fracture characteristics. On the other hand, the secondary cracks on the side surface also fade away and pitting pits appear, indicating a reduction in the SCC sensitivity of the specimen, corresponding to the results of the major fracture. The above fracture results showed that the SCC sensitivity of the specimens decreased with increasing magnetic field strength, with

the lowest SCC sensitivity at 100 mT.

Fig. 12 shows the fracture morphology of the specimens in the solution inoculated with SRB after a fracture. The major fracture of the specimen without a magnetic field showed a large and deep cleavage step, and multiple secondary cracks appeared on the side surfaces (Fig.  $12(a_{1-3})$ ). These characteristics suggested that the fracture mode was a brittle fracture. At a magnetic field strength of 25 mT, Fig.  $12(a_2)$  showed cleavage steps and small cracks, and branching of secondary cracks on the side surfaces, both characteristic of brittle fracture. At 75 mT, the major fracture showed no obvious cleavage steps and exhibited quasi-cleavage features. No cracks were observed on the side surfaces, but pitting pits were found. At 50 mT, the number of pitting pits on the side surfaces was higher, indicating more severe corrosion. Whereas at 100 mT, dimples were visible in the major fracture (Fig.  $12(e_2)$ ), which is typical of ductile fractures. And this was supported by the uniform

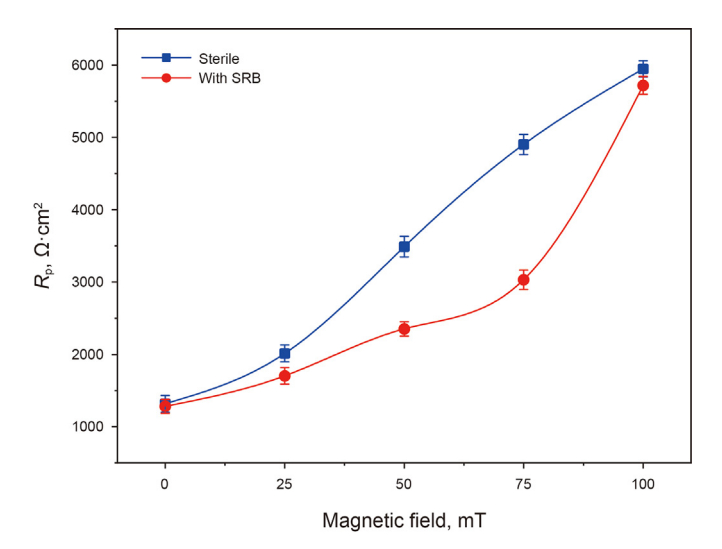


Fig. 8. R<sub>n</sub> values for X80 steel at different magnetic field strengths in sterile and inoculated SRB environments.

corrosion characteristics of the side surfaces (Fig. 12(e<sub>3</sub>)). The specimens in the inoculated SRB environment had the highest SCC sensitivity without a magnetic field. And the SCC sensitivity of the specimens gradually decreased as the magnetic field strength increased, indicating that the magnetic field can inhibit the SCC in the inoculated SRB environment. It was evident in both the major fracture morphologies and the side morphologies, as it was in the sterile solution.

The magnetic field reduced the SCC sensitivity of X80 steel in both sterile and inoculated SRB environments. This suggested that the magnetic field had an inhibiting effect on SCC, but appeared to be somewhat more effective in the sterile environment.

#### 4. Discussion

4.1. The effect of magnetic field on SCC of X80 pipeline steel in a sterile solution

X80 steel is mild steel and is a soft magnetic material (Lee and Lynch, 2000; Krings et al., 2017), Consequently, X80 steel is easily magnetized by the external magnetic field, which affects the surrounding magnetic field distribution. The researchers found symmetrical regions of high magnetic flux density on both sides of the carbon steel under the action of a perpendicular magnetic field (Zhang et al., 2019; Sueptitz et al., 2014; Zhao et al., 2020). Additionally, the magnetic field affects the mass transfer process of corrosion (Hinds et al., 2001; Wang et al., 2014; Yu et al., 2020) mainly through the magnetic field gradient force and Lorentz force (Sueptitz et al., 2009; Monzon and Coey, 2014; Wang et al., 2022). During electrochemical testing the Lorentz force cannot be ignored

Elongation

75

100

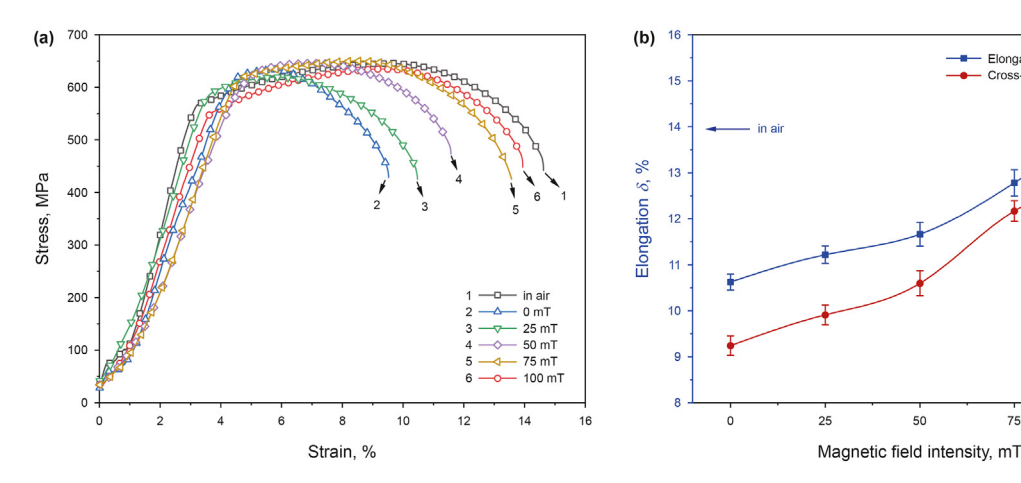


Fig. 9. SSRT results for X80 steel in air and sterile solution at different magnetic field strengths: (a) stress-strain curve; (b) elongation and cross-sectional shrinkage.

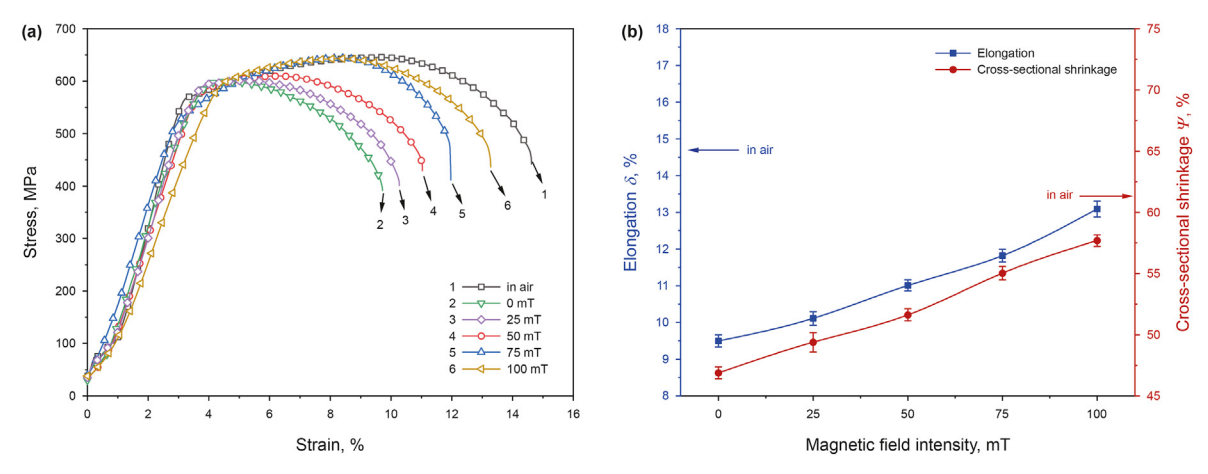


Fig. 10. SSRT results for X80 steel in solution inoculated with SRB at different magnetic field strengths: (a) stress-strain curve; (b) elongation and cross-sectional shrinkage.

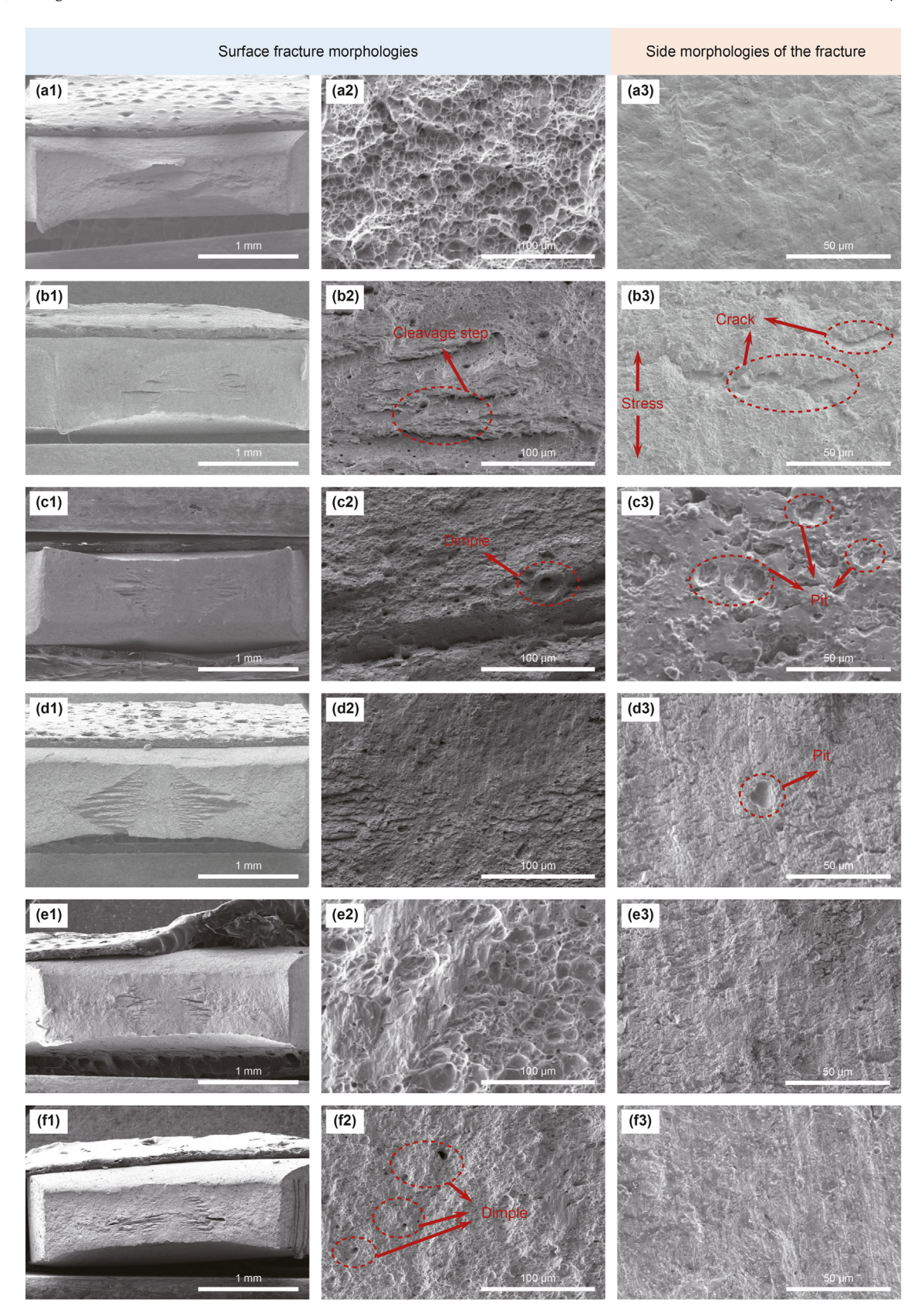


Fig. 11. Fracture morphologies (surface fracture morphologies and side morphologies of the fracture) of X80 steel in sterile solution at different magnetic field strengths:  $(a_{1-3})$  in the air;  $(b_{1-3})$  0 mT;  $(c_{1-3})$  25 mT;  $(d_{1-3})$  50 mT;  $(e_{1-3})$  75 mT;  $(f_{1-3})$  100 mT.

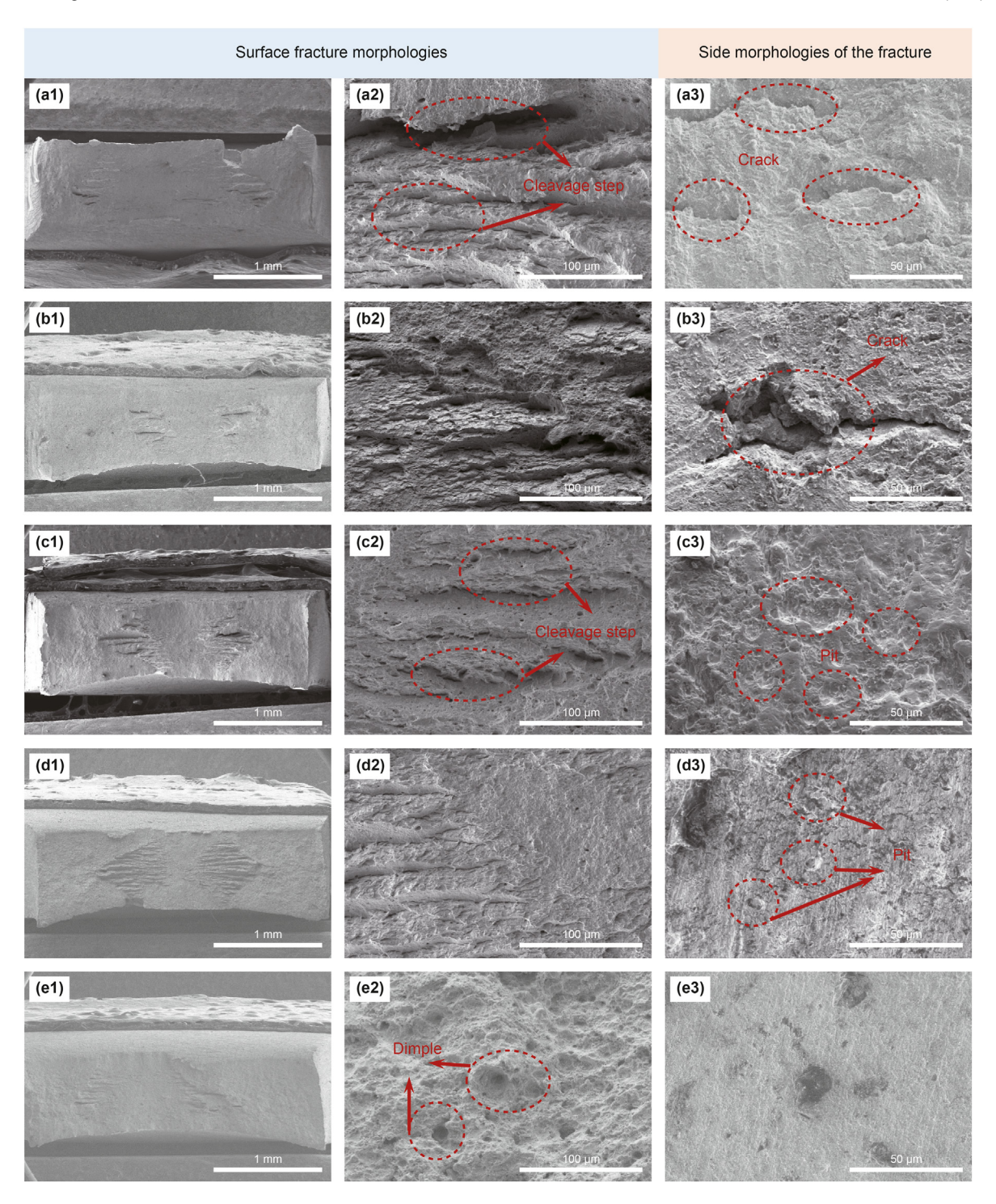


Fig. 12. Fracture morphologies (surface fracture morphologies and side morphologies of the fracture) of X80 steel in solution inoculated with SRB at different magnetic field strengths:  $(\mathbf{a_{1-3}})$  0 mT;  $(\mathbf{b_{1-3}})$  25 mT;  $(\mathbf{c_{1-3}})$  50 mT;  $(\mathbf{d_{1-3}})$  75 mT;  $(\mathbf{e_{1-3}})$  100 mT.

due to the presence of an applied current, the expression for the Lorentz force is as follows.

$$F_{L} = J \times B \tag{4}$$

where J is the energy density of the charged ion, and B is the magnetic field strength. With the application of a magnetic field, the Lorentz force accelerates the mass transport process in the solution. This causes the nutrients in the solution to collect on the

electrode surface, thus preventing the corrosion of the electrode and therefore the impedance becomes larger (Fig.  $7(a_1)$ ). This is also illustrated by the polarization resistance results (Fig. 8). Moreover, the ions in the solution will move faster under the action of Lorentz force, and the corrosion products formed on the electrode surface will be more, thus generating a protective film and reducing the corrosion (Zhang et al., 2019).

High flux density zones exist on both sides of the electrode, so there is a magnetic field gradient near the electrode. And the magnetic field gradient force is mainly related to the magnetic field gradient and particle magnetism (Li et al., 2016). The formula is as follows.

$$F_B = \frac{\chi_{\rm m} c B \, \overline{\nabla} B}{\mu_0} \tag{5}$$

where  $\chi_{\rm m}$  is the magnetization per unit mass, c is the ion concentration,  $\mu_0$  is the absolute magnetic permeability, and  $\overrightarrow{\nabla} B$  is the gradient of magnetic induction.

High magnetic field gradients exist on both sides of the electrode, so the magnetic field gradient force promotes the migration of paramagnetic particles (e.g., Fe<sup>2+</sup>, Fe<sup>3+</sup>, and O<sub>2</sub>) to the vicinity of the electrode. These paramagnetic particles will adsorb to the electrode surface and react to generate more corrosion products to attract to the surface, thus forming a protective film to protect the electrode from corrosion. Additionally, Fe<sup>2+</sup> accumulates near the electrode, limiting the electrolyte transfer at this location, thus preventing the migration of corrosive ions to the electrode surface and inhibiting the corrosion process (Fig. 7(a<sub>1</sub>) and Fig. 8) (Sueptitz et al., 2011). In summary, during the corrosion process, the combined effect of Lorentz force and magnetic field gradient force affects the corrosion product generation and ion migration on the electrode surface, inhibiting the electrochemical corrosion of X80 steel.

SCC cracks, which usually arise from within the pit, generate leakage fields within it under the action of a magnetic field (Zhao et al., 2020). The SCC of X80 pipeline steel is affected by the applied magnetic field and the leakage magnetic field. The magnetic field gradient force is the primary factor controlling the corrosion process without the current (Zhao et al., 2021). The magnetic field gradient force attracts particles such as oxygen and iron chloride to the outside of the defect and hydroxyl ions to the inside of the defect. This results in the formation of an oxide film on the surface of the specimen, mitigating the internal corrosion and thus reducing the SCC sensitivity. This is confirmed by the SSRT results in Fig. 8 and the fracture morphology in Fig. 11.

Meanwhile, the  $I_{SCC}$  was calculated to assess the SCC sensitivity of X80 steel, as shown in Eq. (6) (Torres-Islas and González-Rodríguez, 2009; Sun et al., 2018).

$$I_{\text{SCC}} = \left(1 - \frac{\psi_{\text{sol}}}{\psi_0}\right) \times 100\% \tag{6}$$

where,  $\psi_{sol}$  is the cross-sectional shrinkage of the specimen in the soil simulation solution, and  $\psi_0$  is the cross-sectional shrinkage of the specimen in air. It can be seen from Eq. (6) that if  $\psi_{\text{sol}} < \psi_0$ , then  $I_{SCC}$  is less than 1. And  $I_{SCC}$  is proportional to SCC sensitivity. The  $I_{SCC}$  results are shown in Fig. 13, where the SCC sensitivity in the absence of bacteria gradually decreases with increasing magnetic field strength. During the tensile process, the X80 steel is deformed and geometric discontinuity locations are created at the deformation. After the application of an external magnetic field, the magnetic field strength is higher at the edge locations of the geometric discontinuities, and paramagnetic particles such as Fe<sup>2+</sup> and O<sub>2</sub> accumulate at these locations, while antimagnetic ions such as the corrosive ion Cl- tend to move away from these locations (Yang et al., 2022). Therefore, an oxide film is generated on the surface of X80 steel, which protects the steel matrix from corrosion attack. Thus, the SCC sensitivity is reduced (Fig. 13). According to Eq. (5), the magnetic field gradient force is proportional to the magnetic field strength. Consequently, the magnetic field gradient force increases with increasing magnetic field strength, allowing paramagnetic particles to aggregate faster on

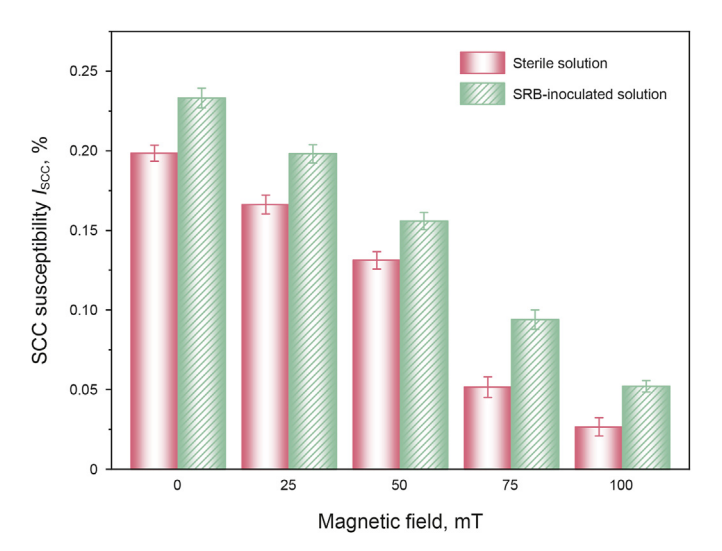


**Fig. 13.** SCC sensitivity ( $I_{SCC}$ ) results calculated for X80 steel at different magnetic field strengths in sterile and inoculated SRB environments.

the steel surface, speeding up film formation and reducing the SCC sensitivity (Fig. 13).

Fig. 14 shows the EDS results for the side surfaces of specimens after fracturing under a sterile environment. After applying a magnetic field, the elemental iron content on the side surface of the specimen increased. It suggests that the metal matrix does not undergo a violent corrosion reaction and that the corrosion level is low, therefore SCC sensitivity is demonstrated to be much lower, validating the results in Fig. 13.

#### 4.2. Effect of SRB on SCC of X80 pipeline steel

SRB is an important cause of metal pitting and SCC cracking originated from pitting (Videla et al., 2001; Anandkumar et al., 2016). Additionally, SRB strains, sulfides, and EPS adsorb to the metal surface to form films (Fig. 6), changing the physicochemical parameters of the metal interface and thus affecting the corrosion process (Dong et al., 2011).

Recently, researchers presented the "Biocathodic Sulfate Reduction Theory (BCSR)" (shown in the top right corner of Fig. 16) (Gu et al., 2009; Xu and Gu, 2014; Li et al., 2018), which describes the corrosion process of microorganisms in terms of film layer under bioenergetics. According to the theory, microorganisms catch the electrons produced by metal dissolution via the film adhered to the metal surface and get the energy required to continue life, resulting in corrosion, in the following reaction.

Anodic reaction:

$$Fe \rightarrow Fe^{2+} + 2e^{-} \tag{7}$$

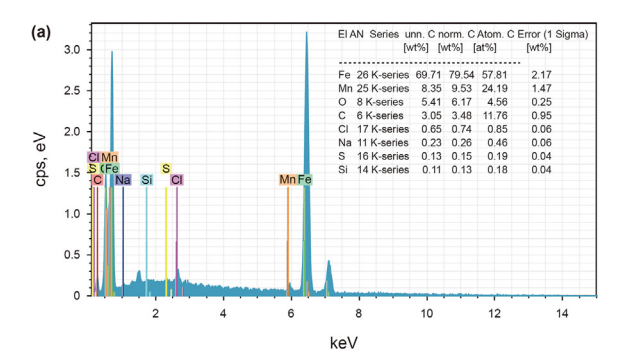
Cathodic reaction:

$$SO_4^{2-} + 9H^+ + 8e^- \rightarrow HS^- + 4H_2O$$
 (8)

Total reaction:

$$4Fe + SO_4^{2-} + 9H^+ \rightarrow HS^- + 4H_2O + 4Fe^{2+}$$
 (9)

The surface of the metal is covered with a film after immersion, as shown in Fig. 6. According to the BCSR theory, Fe can perform as an electron donor for SRB under the film, inducing electrochemical reactions at the metal-film interface and intensifying the local



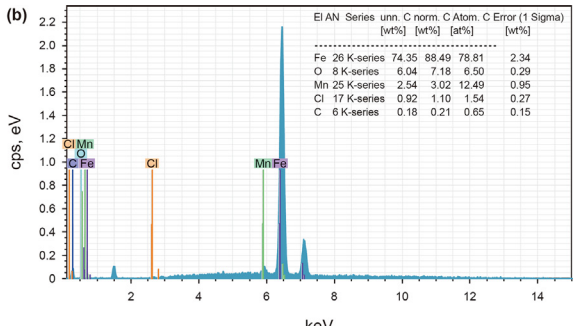


Fig. 14. EDS results of fractured X80 steel specimens in the sterile environment: (a) 0 mT; (b) 100 mT.

corrosion (pitting) on the metal surface. Tensile stresses cause stress concentrations at the bottom of pits or localized corrosion during tensile testing, eventually leading to SCC on the specimen's surface. The majority of SCC cracks have been reported to form near the base of pits on metal surfaces (Bouaeshi et al., 2007; Zhu et al., 2013). SRB intensifies pitting on the metal surface by the action of the film, which leads to the increase of SCC sensitivity. This is also illustrated by the results of the  $I_{\rm SCC}$  comparison between sterile and bacterial in Fig. 13. Also as shown in Figs. 9 and 10, cross-sectional shrinkage and elongation in the SRB environment were lower than in the sterile environment and in the air, further illustrating the promotion of SRB for the SCC of X80 steel.

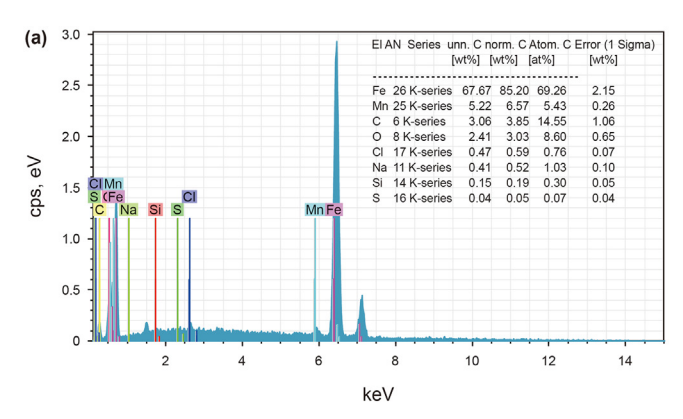
## 4.3. The SCC mechanism of X80 pipeline steel in the coexistence of magnetic field and SRB

When the magnetic field and SRB are present simultaneously, the magnetic field affects the growth and metabolism of SRB, which further influences the SCC behavior of the metal. Firstly, the magnetic field leads to a reduction of SRB adsorbed on the surface of the specimen (Fig. 5), which prevents the SRB from corroding the metal (Fig. 5). The reasons for this outcome are multiple. The stronger the magnetic field, the more effective the inhibition (Fig. 6). Bacterial cell membranes contain numerous anisotropic molecules with antimagnetic characteristics. When a magnetic field is loaded, the antimagnetic molecules rotate and the ion channels within the cell membrane are altered, which in turn affects the ion exchange inside and outside the cell membrane. As a result, bacteria's regular growing and metabolic processes are impacted (Ji et al., 2009;

Letuta and Berdinskiy, 2017), which lowers their activity. Additionally, proteins and enzymes that contain paramagnetic materials in SRBs are impacted by magnetic fields (Chua and Yeo, 2005; Kroupová et al., 2007; Filipič et al., 2012), resulting in a decrease in SRB, which also aids in inhibiting corrosion.

Secondly, the film layer adsorbed on the specimen's surface is also affected by the magnetic field. In the absence of a magnetic field, the surface of the specimen adsorbs a complex product film composed of additional components such as SRB, EPS, and corrosion products (e.g., Fig.  $6(a_1)$ ), but the film is not uniform or dense enough to provide an effective shielding effect on the steel matrix. Aggressive ions could spread through cracks, speeding up the corrosion of metal surfaces. Both of these effects would trigger local corrosion and pit on the surface of the specimen. The smallest semicircle diameter in the impedance spectrum (Fig. 7(b<sub>1</sub>)) might also be connected to the non-uniform film without a magnetic field. When a magnetic field is provided, the film on the specimen surface became denser than when no magnetic field was applied (Fig. 6(e)), and the cracks essentially disappear, giving more efficient shielding to the steel matrix. The film becomes denser as the magnetic field strength increases.

The results of the film layer's EDS analysis (Fig. 6(a<sub>2</sub>) and (e<sub>2</sub>)) also suggest that the film's iron sulfide content increases because of the magnetic field. Iron sulfide tends to become magnetized by the magnetic field, which makes it adhere more strongly to the specimen's surface. Together with the adhesive effect of the EPS secreted by the SRB, the EPS and iron sulfide will form a tighter and more homogeneous film on the surface of the specimen, protecting the steel matrix from aggressive ions. The type and orientation of



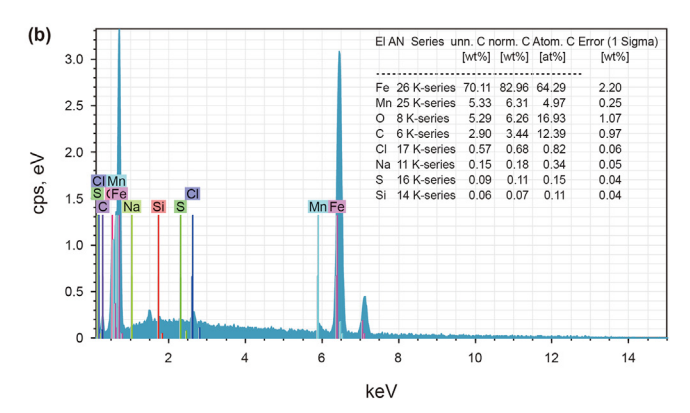


Fig. 15. EDS results of fractured X80 steel specimens in the inoculated SRB environment: (a) 0 mT; (b) 100 mT.

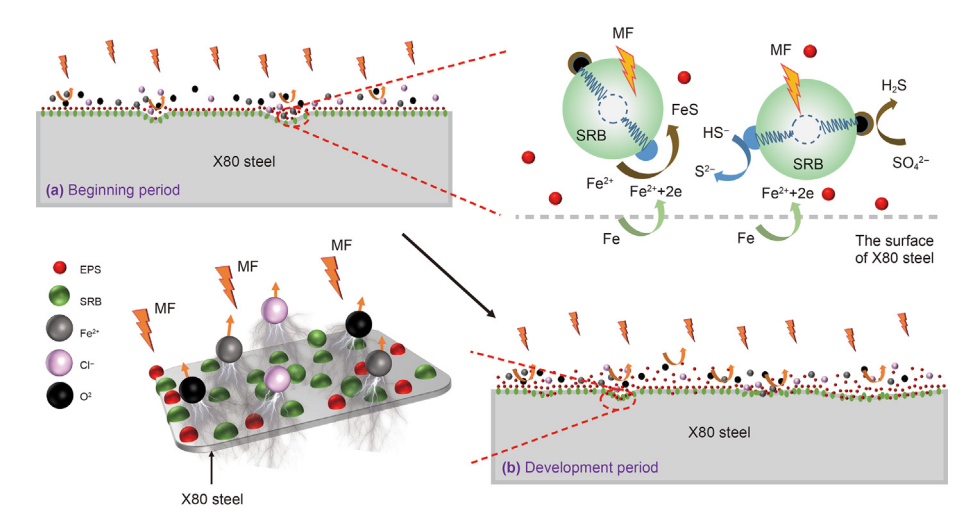


Fig. 16. The SCC mechanism of X80 steel in the coexistence of magnetic field and SRB environments.

corrosion products were also found to be influenced by magnetic fields (Liu et al., 2016). Magnetic fields cause a single type of corrosion product to be generated and grow in the same direction, resulting in a denser corrosion product film and better protection for the steel matrix.

The energy spectra of the side surfaces of the specimens with and without an applied 100 mT magnetic field are compared (Fig. 15). This result is similar to Fig. 14, which laterally verifies that the magnetic field in the SRB environment also has an inhibitory effect on SCC.

The magnetic field not only inhibits the growth of SRB on the metal surface but also makes the surface film of the specimen denser. The two effects together reduce the pitting and SCC sensitivity of X80 steel specimens (as shown in Fig. 13). Fig. 16 illustrates the corrosion mechanism under conditions of coexistence of magnetic field and SRB. After the external magnetic field is applied, the number of SRB on the surface of X80 steel is reduced and the magnetization causes a dense protective film to form on the steel surface, which protects the metal matrix. In addition, the magnetic field force keeps the corrosive ions away from the X80 steel. These aspects work together to reduce the probability of localized corrosion occurring in X80 steel, thus reducing the SCC sensitivity. Because the specific mechanisms of action of magnetic fields on bacteria are still complex, more research into the impact of magnetic fields on bacterial physiological activity is required to elucidate in greater detail the process of microbial corrosion with a magnetic field.

#### 5. Conclusion

In this paper, the SCC behavior of X80 pipeline steel under the coexistence of perpendicular magnetic field and SRB in the soil environment was investigated. The number of SRB cells on the surface of X80 steel specimens decreased with increasing perpendicular magnetic field strength and the perpendicular magnetic field promoted the formation of a denser film. The magnetic fields inhibit SCC in the abiotic and SRB environment.

This study is instructive for the safe operation of buried pipelines, where leakage magnetic detection not only detects defects in pipelines, but also inhibits microbial growth as well as microbial corrosion. This is of great significance for the future application of leakage magnetic detection technology.

#### **Declaration of competing interest**

The authors declare that they have no known competing financial interests or personal relationships that could have appeared to influence the work reported in this paper.

#### Acknowledgments

This project was supported by the National Science Foundation of China (Grant numbers 52274062) and Natural Science Foundation of Liaoning Province (Grant numbers 2022-MS-362).

#### References

Anandkumar, B., George, R.P., Maruthamuthu, S., et al., 2016. Corrosion characteristics of sulfate-reducing bacteria (SRB) and the role of molecular biology in SRB studies: an overview. Corrosion Rev. 34, 41–63. https://doi.org/10.1515/corrrev-2015-0055

Bouaeshi, W., Ironside, S., Eadie, R., 2007. Research and cracking implications from an assessment of two variants of near-neutral pH crack colonies in liquid pipelines. Corrosion 63, 648–660. https://doi.org/10.5006/1.3278415.

Chen, B., Liu, H.W., Wu, Y.N., et al., 2014. Influence of static magnetic field on microbiologically induced corrosion of Cu-Zn alloy in SRB culture medium. ECS Trans. 59. 439. https://doi.org/10.1149/05901.0439ecst.

Cheng, Y.F., 2013. Understanding pipeline stress corrosion cracking. Stress corrosion cracking of pipelines 46, 631–638. https://doi.org/10.1002/9781118537022.ch3.

Chua, L.Y., Yeo, S.H., 2005. Surface bio-magnetism on bacterial cells adhesion and surface proteins secretion. Colloids Surf., B 40, 45–49. https://doi.org/10.1016/ i.colsurfb.2004.10.004.

Dong, Z.H., Shi, W., Ruan, H.M., et al., 2011. Heterogeneous corrosion of mild steel under SRB-biofilm characterised by electrochemical mapping technique. Corrosion Sci. 53, 2978–2987. https://doi.org/10.1016/j.corsci.2011.05.041.

Dou, W., Jia, R., Jin, P., et al., 2018. Investigation of the mechanism and characteristics of copper corrosion by sulfate reducing bacteria. Corrosion Sci. 144, 237–248. https://doi.org/10.1016/j.corsci.2018.08.055.

Filipič, J., Kraigher, B., Tepuš, B., et al., 2012. Effects of low-density static magnetic fields on the growth and activities of wastewater bacteria Escherichia coli and Pseudomonas putida. Bioresour. Technol. 120, 225–232. https://doi.org/ 10.1016/J.BIORTECH.2012.06.023.

Fojt, L., Strašák, L., Vetterl, V., 2010. Extremely-low frequency magnetic field effects on sulfate reducing bacteria viability. Electromagn. Biol. Med. 29, 177–185. https://doi.org/10.3109/15368378.2010.513304.

Gong, K., Wu, M., Liu, G.X., 2020. Stress corrosion cracking behavior of rusted X100 steel under the combined action of Cl and HSO<sub>3</sub> in a wet-dry cycle environment. Corrosion Sci. 165. https://doi.org/10.1016/j.corsci.2019.108382.

Gu, T., Zhao, K., Nesic, S., 2009. A new mechanistic model for MIC based on a biocatalytic cathodic sulfate reduction theory. In: NACE-09390, International Corrosion Conference Series.

Hinds, G., Coey, J., Lyons, M., 2001. Influence of magnetic forces on electrochemical mass transport. Electrochem. Commun. 3, 215–218. https://doi.org/10.1016/ S1388-2481(01)00136-9.

Jackson, J.E., Lasseigne-Jackson, A.N., Sanchez, F.J., et al., 2006. The influence of magnetization on corrosion in pipeline steels. Integrity Management; Poster

Session; Student Paper Competition. In: Proceedings of the 2006 International Pipeline Conference, vol. 2. ASME, Calgary, Alberta, Canada, pp. 921–929. https://doi.org/10.1115/IPC2006-10615.

- Javidi, M., Bahalaou Horeh, S., 2014. Investigating the mechanism of stress corrosion cracking in near-neutral and high pH environments for API 5L X52 steel. Corrosion Sci.: The Journal on Environmental Degradation of Materials and its Control 80, 213—220. https://doi.org/10.1016/j.corsci.2013.11.031.
- Ji, W., Huang, H., Deng, A., et al., 2009. Effects of static magnetic fields on Escherichia coli. Micron 40, 894–898. https://doi.org/10.1016/j.micron.2009.05.010.
- Krings, A., Boglietti, A., Cavagnino, A., et al., 2017. Soft magnetic material status and trends in electric machines. IEEE Trans. Ind. Electron. 64, 2405–2414. https:// doi.org/10.1109/TIE.2016.2613844.
- Kroupová, J., ártová, E.B., Fojt, L., et al., 2007. Low-frequency magnetic field effect on cytoskeleton and chromatin. Bioelectrochemistry 70, 96–100. https://doi.org/ 10.1016/j.bioelechem.2006.03.034.
- Lee, E.W., Lynch, A.C., 2000. Soft magnetic materials. China Rare Earth Information 78, 947–972. https://doi.org/10.1109/5.56909.
- Letuta, U.G., Berdinskiy, V.L., 2017. Magnetosensitivity of bacteria E. coli: magnetic isotope and magnetic field effects. Bioelectromagnetics 38, 581–591. https://doi.org/10.1002/bem.22073.
- Li, X., Zhang, M., Yuan, B., et al., 2016. Effects of the magnetic field on the corrosion dissolution of the 304 SS[FeCl<sub>3</sub> system. Electrochim. Acta 222, 619–626. https://doi.org/10.1016/j.electacta.2016.11.017.
- Li, Y., Xu, D., Chen, C., et al., 2018. Anaerobic microbiologically influenced corrosion mechanisms interpreted using bioenergetics and bioelectrochemistry: a review. J. Mater. Sci. Technol. 34, 1713–1718. https://doi.org/10.1016/j.jmst.2018.02.023.
- Li, J.H., Xie, F., Wang, D., et al., 2021. Effect of magnetic field on stress corrosion cracking induced by Sulfate-reducing bacteria. Construct. Build. Mater. 303. https://doi.org/10.1016/j.conbuildmat.2021.124521.
   Liu, H.W., Cheng, Y.F., 2020. Corrosion of X52 pipeline steel in a simulated soil so-
- Liu, H.W., Cheng, Y.F., 2020. Corrosion of X52 pipeline steel in a simulated soil solution with coexistence of Desulfovibrio desulfuricans and Pseudomonas aeruginosa bacteria. Corrosion Sci. 173, 108753. https://doi.org/10.1016/i.corsci.2020.108753.
- Liu, H., Gu, T., Zhang, G., et al., 2016. The effect of magnetic field on biomineralization and corrosion behavior of carbon steel induced by iron-oxidizing bacteria. Corrosion Sci. 102, 93–102. https://doi.org/10.1016/j.corsci.2015.09.023.
- Liu, Z.Y., Li, Q., Cui, Z.Y., et al., 2017. Field experiment of stress corrosion cracking behavior of high strength pipeline steels in typical soil environments. Construct. Build. Mater. 148, 131–139. https://doi.org/10.1016/ i.conbuildmat.2017.05.058.
- Liu, H.W., Xu, D.K., Zheng, B.J., et al., 2018. A synergistic acceleration of corrosion of Q235 carbon steel between magnetization and extracellular polymeric substances. Acta Metallurgica Sinica-English Letters 31, 456–464. https://doi.org/ 10.1007/s40195-017-0666-4.
- Lu, Z., Shoji, T., Yang, W., 2010. Anomalous surface morphology of iron generated after anodic dissolution under magnetic fields. Corrosion Sci. 52, 2680–2686. https://doi.org/10.1016/j.corsci.2010.04.019.
- Ma, H., Zhao, B., Liu, Z., et al., 2020. Local chemistry-electrochemistry and stress corrosion susceptibility of X80 steel below disbonded coating in acidic soil environment under cathodic protection. Construct. Build. Mater. 243, 118203. https://doi.org/10.1016/j.conbuildmat.2020.118203.
- Monzon, L.M., Coey, J.M.D., 2014. Magnetic fields in electrochemistry: the Lorentz force. A mini-review. Electrochem. Commun. 42, 38–41. https://doi.org/ 10.1016/j.elecom.2014.02.006.
- Niazi, H., Eadie, R., Chen, W., et al., 2021. High pH stress corrosion cracking initiation and crack evolution in buried steel pipelines: a review. Eng. Fail. Anal. 120, 105013. https://doi.org/10.1016/j.engfailanal.2020.105013.
- Parapurath, S., Ravikumar, A., Vahdati, N., et al., 2021. Effect of magnetic field on the corrosion of API-5L-X65 steel using electrochemical methods in a flow loop. Appl. Sci. 11, 9329. https://doi.org/10.3390/app11199329.
- Ramamurthy, S., Atrens, A., 2013. Stress corrosion cracking of high-strength steels. Corrosion Rev. 31, 1–31. https://doi.org/10.1002/srin.200100132.
- Ručinskien, A., Bikulčius, G., Gudavičiūt, L., et al., 2002. Magnetic field effect on stainless steel corrosion in FeCl<sub>3</sub> solution. Electrochem. Commun. 4, 86–91. https://doi.org/10.1016/S1388-2481(01)00280-6.
- Song, F., 2010. Predicting the effect of soil seasonal change on stress corrosion cracking susceptibility of buried pipelines at high pH. Corrosion 66 (9), 095004–095004-14. https://doi.org/10.5006/1.3490309.
- Su, S., Wang, P., Shi, P., et al., 2022. Experiment and simulation on testing steel plate with corrosion defects via magnetic flux leakage method. J. Magn. Magn Mater. 560, 169595. https://doi.org/10.1016/j.jmmm.2022.169595.
- Sueptitz, R., Koza, J., Uhlemann, M., et al., 2009. Magnetic field effect on the anodic behaviour of a ferromagnetic electrode in acidic solutions. Electrochim. Acta 54, 2229–2233. https://doi.org/10.1016/j.electacta.2008.10.055.
- Sueptitz, R., Tschulik, K., Uhlemann, M., et al., 2011. Effect of high gradient magnetic fields on the anodic behaviour and localized corrosion of iron in sulphuric acid solutions. Corrosion Sci. 53, 3222–3230. https://doi.org/10.1016/j.corsci.2011.05.070.
- Sueptitz, R., Tschulik, K., Uhlemann, M., et al., 2014. Retarding the corrosion of iron

- by inhomogeneous magnetic fields. Mater. Corros. 65, 803–808. https://doi.org/10.1002/maco.201206890.
- Sun, D.X., Wu, M., Xie, F., 2018. Effect of sulfate-reducing bacteria and cathodic potential on stress corrosion cracking of X70 steel in sea-mud simulated solution. Mater. Sci. Eng., A 721, 135–144. https://doi.org/10.1016/j.msea.2018.02.007.
- Torres-Islas, A., González-Rodríguez, J., 2009. Effect of electrochemical potential and solution concentration on the SCC behaviour of X-70 pipeline steel in NaHCO<sub>3</sub>. Int. J. Electrochem. Sci. 4, 640–653. https://doi.org/10.1016/j.electacta.2009.01.013.
- Unsal, T., Wang, D., Kumseranee, S., et al., 2021. d-Tyrosine enhancement of microbiocide mitigation of carbon steel corrosion by a sulfate reducing bacterium biofilm. World J. Microbiol. Biotechnol. 37, 103. https://doi.org/10.1007/ s11274-021-03072-9.
- Videla, H.A., Edyvean, R.G., Archer, E.D., et al., 2001. Selection of Steels for Use in SRB Environments. CORROSION, Houston, Texas,. March 2001.
- Wan, H., Song, D., Du, C., et al., 2019. Effect of alternating current and Bacillus cereus on the stress corrosion behavior and mechanism of X80 steel in a Beijing soil solution. Bioelectrochemistry 127, 49–58. https://doi.org/10.1016/j.bioelechem.2019.01.006.
- Wang, X., Zhao, J., Hu, Y., et al., 2014. Effects of the Lorentz force and the gradient magnetic force on the anodic dissolution of nickel in HNO<sub>3</sub> + NaCl solution. Electrochim. Acta 117, 113—119. https://doi.org/10.1016/j.electacta.2013.11.100.
- Wang, D., Xie, F., Wu, M., et al., 2017. Stress corrosion cracking behavior of X80 pipeline steel in acid soil environment with SRB. Metall. Mater. Trans. A 48A, 2999–3007. https://doi.org/10.1007/s11661-017-4068-z.
- Wang, Z.Q., Xie, F., Wang, D., et al., 2021. Effect of applied potential on stress corrosion cracking behavior of X80 steel in alkaline soil simulated solution with sulfate-reducing bacteria. Eng. Fail. Anal. 121. https://doi.org/10.1016/j.engfailanal.2020.105109.
- Wang, D., Li, T., Xie, F., et al., 2022. Effect of magnetic field on the electrochemical corrosion behavior of X80 pipeline steel. Construct. Build. Mater. 350, 128897. https://doi.org/10.1016/j.conbuildmat.2022.128897.
   Wei, B., Xu, J., Cheng, Y.F., et al., 2021. Effect of uniaxial elastic stress on corrosion of
- Wei, B., Xu, J., Cheng, Y.F., et al., 2021. Effect of uniaxial elastic stress on corrosion of X80 pipeline steel in an acidic soil solution containing sulfate-reducing bacteria trapped under disbonded coating. Corrosion Sci. 193, 109893. https://doi.org/ 10.1016/j.corsci.2021.109893.
- Wu, T., Xu, J., Yan, M., et al., 2014. Synergistic effect of sulfate-reducing bacteria and elastic stress on corrosion of X80 steel in soil solution. Corrosion Sci. 83, 38–47. https://doi.org/10.1016/j.corsci.2014.01.017.
- Xian, H.Q., Guo, L.Z., Zha, K.Q., et al., 2010. Microbiology Experiment Tutorial. Higher Education Press, Beijing (in Chinese).
- Xie, F., Li, J.H., Zou, T., et al., 2021. Stress corrosion cracking behavior induced by Sulfate-reducing bacteria and cathodic protection on X80 pipeline steel. Construct. Build. Mater. 308. https://doi.org/10.1016/j.conbuildmat.2021.125093.
- Xu, D., Gu, T., 2014. Carbon source starvation triggered more aggressive corrosion against carbon steel by the Desulfovibrio vulgaris biofilm. Int. Biodeterior. Biodegrad. 91, 74–81. https://doi.org/10.1016/j.ibiod.2014.03.014.
- Yang, J., Wang, Z.B., Qiao, Y.X., et al., 2022a. Synergistic effects of deposits and sulfate reducing bacteria on the corrosion of carbon steel. Corrosion Sci. 199, 110210. https://doi.org/10.1016/j.corsci.2022.110210.
- Yang, Y., Zhang, Q.B., Zhu, W.C., et al., 2022b. Effect of magnetic field on corrosion behavior of X52 pipeline steel in NaCl solution. J. Chin. Soc. Corrosion Protect 42, 501–506. https://doi.org/10.11902/1005.4537.2021.117.
- Yu, X., Wang, Z., Lu, Z., 2020. Atmospheric corrosion behavior of copper under static magnetic field environment. Mater. Lett. 266, 127472. https://doi.org/10.1016/ i.matlet.2020.127472.
- Zhang, Y., Wang, Y., Zhao, S., et al., 2019. Effect of magnetic field on the corrosion behaviour of carbon steel in static seawater. Int. J. Electrochem. Sci. 14, 11279—11288. https://doi.org/10.20964/2019.12.14.
- Zhang, X., Wang, Z., Zhou, Z., et al., 2021. Impact of magnetic field on corrosion performance of Al-Mg alloy with different electrode potential phases. Intermetallics 129, 107037. https://doi.org/10.1016/j.intermet.2020.107037.
- Zhao, S., Wang, Y., Zhao, Y., et al., 2020b. The effect of magnetic field pretreatment on the corrosion behavior of carbon steel in static seawater. RSC Adv. 10, 2060–2066. https://doi.org/10.1039/C9RA09079G.
- Zhao, S.L., Bai, J.J., You, Z.F., et al., 2020b. Effect of a magnetic field on stress corrosion cracking of Fe<sub>83</sub> Ga<sub>17</sub> alloy. Corrosion Sci. 167. https://doi.org/10.1016/ j.corsci.2020.108539.
- Zhao, S.L., You, Z.F., Zhang, X.W., et al., 2021. Magnetic field effects on the corrosion and electrochemical corrosion of Fe<sub>83</sub>Ga<sub>17</sub> alloy. Mater. Char. 174. https://doi.org/10.1016/j.matchar.2021.110994.
- Zheng, B.J., Li, K.J., Liu, H.F., et al., 2014. Effects of magnetic fields on microbiologically influenced corrosion of 304 stainless steel. Ind. Eng. Chem. Res. 53, 48–54. https://doi.org/10.1021/ie402235j.
- Zhu, L.K., Yan, Y., Qiao, L.J., et al., 2013. Stainless steel pitting and early-stage stress corrosion cracking under ultra-low elastic load. Corrosion Sci. 77, 360–368. https://doi.org/10.1016/j.corsci.2013.08.028.